

Heisenberg-Limited Waveform Estimation with Solid-State Spins in Diamond

Yang Dong,^{1,2} Ze-Hao Wang,^{1,2} Hao-Bin Lin,^{1,2} Shao-Chun Zhang,^{1,2} Yu Zheng,^{1,2} Xiang-Dong Chen,^{1,2} Wei Zhu,³ Guan-Zhong Wang,³ Guang-Can Guo,^{1,2} and Fang-Wen Sun^{1,2,*}

¹CAS Key Laboratory of Quantum Information, University of Science and Technology of China, Hefei, 230026, P.R. China

²CAS Center for Excellence in Quantum Information and Quantum Physics, University of Science and Technology of China, Hefei, 230026, P.R. China

³Hefei National Laboratory for Physical Science at Microscale, and Department of Physics, University of Science and Technology of China, Hefei, Anhui 230026, P. R. China

(Dated: May 14, 2021)

The newly established Heisenberg limit in arbitrary waveform estimation is quite different with parameter estimation and shows a unique characteristic of a future quantum version of oscilloscope. However, it is still a non-trivial challenge to generate a large number of exotic quantum entangled states to achieve this quantum limit. Here, by employing the time-domain quantum difference detection method, we demonstrate Heisenberg-limited waveform quantum estimation with diamond spins under ambient condition in the experiment. Periodic dynamical decoupling is applied to enhance both the dynamic range and sensitivity by one order of magnitude. Using this quantum-enhanced estimation scheme, the estimation error of an unknown waveform is reduced by more than 5 dB below the standard quantum limit with $N \sim 2 \times 10^3$ resources, where more than 1×10^5 resources would be required to achieve a similar error level using classical detection. This work provides an essential step towards realizing quantum-enhanced structure recognition in a continuous space and time.

Quantum metrology [1–8] takes its superpower from superposition [9, 10] and entanglement [11–13] to yield higher statistical precision than pure classical approaches. And the Heisenberg quantum limit (HQL) measurement ($\delta = O(N^{-1})$) totally outperforms the standard quantum limit (SQL) ($\delta = O(N^{-1/2})$), where N is the number of resources. Over the last few decades, lots of experimental systems, such as multi-photon interferometers [4, 14–16], trapped ions [17, 18], superconducting circuits [19], and solid-spin [7, 20, 21], exploited quantum entanglement to demonstrate this non-classical sensitivity. To extend current results for widely high precision metrology applications, it is natural to consider the continuous [22–26] nature of the detected signal, which can be categorized as an arbitrary waveform estimation to further construct a quantum version of oscilloscope. Unlike scalar and vector estimation [1–7], arbitrary waveform estimation involves infinite degrees of freedom. Theoretically, the statistical error is bounded by the HQL of $O(N^{-q/(q+1)})$ over the SQL of $O(N^{-q/(2q+1)})$ to demonstrate the quantum superiority [23], where q is a measure of the degree of smoothness of the waveform. It is significantly different with quantum-enhanced parameter estimation [1–7]. This is a milestone in quantum metrology which will be further applied in the efficient detection of functional structures—continuous physical signal including the detection of the nanoscale nuclear magnetic resonance [22–24, 27], nano-materials [28, 29], event horizons [30, 31], and living cell based on quantum systems.

In the canonical form of quantum-enhanced metrology, achieving HQL scaling for such a waveform estimation usually requires the use of large size exotic quan-

tum entangled states [2, 23, 32–34], which is still a non-trivial challenge with currently available quantum technology [1–3, 6, 35]. In this work, we experimentally demonstrate an HQL arbitrary reproducible waveform estimation based on the time-domain quantum difference (TDQD) protocol with the electron spin of nitrogen-vacancy (NV) center in diamond. The basic idea is to use a multi-pass scheme [6] to coherently amplify the unknown detection signal, cancel unwanted coherent dynamical evolution and suppress quantum decoherence simultaneously. By combing with periodic dynamical decoupling (PDD) method, both dynamic range and sensitivity for waveform estimation are improved by one order of magnitude [25]. Finally, the scaling law of HQL for waveform estimation is achieved in the experiment with such a PDD-enhanced TDQD protocol, which significantly beats the results of SQL by more than 5 dB and demonstrates the unique characteristic of the quantum version of oscilloscope.

In general, we consider the estimation of an unknown waveform $b(t)$ defined over an interval $t \in [0, T]$ with a quantum probe, where $b(t)$ can be stored in a relative phase $\phi(t)$ of its quantum state and sampled using an impulse train of n_1 impulses, as shown in Fig. 1. The phase $\phi(t_i)$ at each moment t_i is measured by n_2 resources. Finally, we can conveniently generate the waveform estimator $\tilde{\phi}(t)$ with the individual estimators $\phi(t_i)$ by a zero-order hold method [23, 24, 36]: $\tilde{\phi}(t) = \sum_{i=1}^{n_1} \phi(t_i) \theta(t - t_i)$, where θ is a smoothing function with $\theta(t) = 1$ for $|t| \leq T/2n_1$ and $\theta(t) = 0$ otherwise. For a given stochastic estimator $\tilde{\phi}$, the waveform estimation error [23] (see Supplemental Material for de-

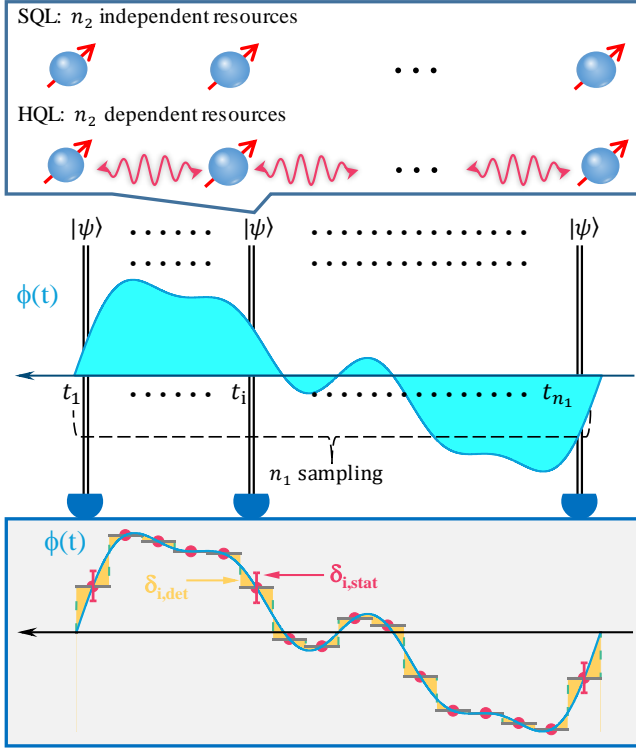


FIG. 1. Conceptual diagrams for waveform estimation with n_1 samplings and n_2 independent or correlated quantum resources. The total error includes the deterministic error (golden shadow) and statistical error (red error bar).

tails [37]) can be directly decomposed into two parts

$$\delta^2 = \delta_{det}^2 + \delta_{stat}^2, \quad (1)$$

where δ_{stat} is the statistical error caused by the quantum projection measurement, and δ_{det} is the deterministic error caused by the smoothing process, as shown in Fig. 1. When the waveform is q th-order differentiable, $\delta_{det} = O(n_1^{-q})$ [23, 37]. And standard measurement schemes using each resource independently lead to a classical phase uncertainty that scales as $\delta_{stat} = O(n_2^{-1/2})$. While, by employing quantum correlations [1–3, 6], the quantum enhanced measurements toward $\delta_{stat} = O(n_2^{-1})$ will be available. Hence, for a given total number of quantum resources $N = n_1 n_2$, the optimal measurement is determined by the trade-off between these two errors. By employing the inequality of arithmetic and geometric means, the estimation error of arbitrary waveform is bounded by the SQL of $\delta = O(N^{-q/(2q+1)})$ and the HQL of $\delta = O(N^{-q/(q+1)})$ [23, 37]. For the present case $q = 1$, the optimal allocation of quantum resource for the best arbitrary waveform estimation can be realized with $n_1 = O(N^{1/3})$, $n_2 = O(N^{2/3})$ for SQL scheme and $n_1 = O(N^{1/2})$, $n_2 = O(N^{1/2})$ for HQL scheme.

Here, we experimentally demonstrate the arbitrary reproducible waveform estimation with the negatively

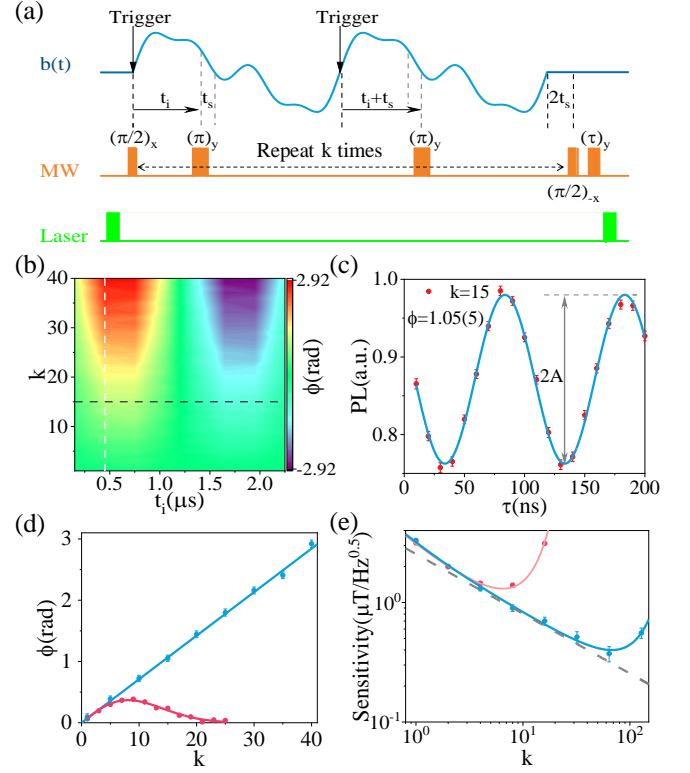


FIG. 2. (a) PDD-enhanced TDQD protocol for arbitrary reproducible waveform detection with NV center. (b) The detection of a sinusoidal waveform $b(t) = b \sin \omega t$ with a period of $T = 2.4 \mu s$. The integration time is $t_s = 300$ ns and π -pulse duration is $t_\pi = 50$ ns. (c) The readout of unknown phase with Rabi oscillation with $k = 15$ and $t_i = 450$ ns, corresponding to the intersection of white and black dashed lines in Fig. 2(b). (d) The accumulation phase as a function of k with the PDD-enhanced (blue circles) and normal [25] (red circles) TDQD protocols. Lines are theoretical results. With the PDD-enhanced TDQD protocol, the solid blue line shows a linear scaling. The uncertainty of phase estimation [5, 7, 41] (error bars) is calculated in a simple way $\Delta\phi_k = \frac{\sigma}{A}$, where σ is signal fluctuation and A is the amplitude of Rabi oscillation as shown in Fig. 2(c). (e) The sensitivity of waveform estimation with the PDD-enhanced (blue circles) and normal (red circles) TDQD protocol. Without taking the decoherence into consideration, the sensitivity scales as the dashed gray line. The best experimental sensitivity (blue dots) is $370 \text{ nT}/\sqrt{Hz}$ for $k = 64$.

charged NV center in diamond [10, 37, 41–44], where a substitutional nitrogen atom is next to a vacancy, forming a spin triplet system in its ground state. A room-temperature home-built confocal microscopy is employed to image, initialize and read out the NV center in a single-crystal synthetic diamond sample, which is mounted on a three-axis closed-loop piezoelectric stage for sub-micrometer-resolution scanning. Fluorescence photons are collected into a fiber and detected using single-photon counting module. A copper wire of $10 \mu m$ diameter above on the bulk diamond is used for the delivery of microwave

(MW) and waveform to the NV center. The optical and MW pulse sequences are synchronized by a multichannel pulse generator. Single NV centers are identified by observing anti-bunching in photon correlation measurements.

We perform the waveform estimation by employing a PDD-enhanced TDQD protocol which is based on the differential spin-echo detection [25], as shown in Fig. 2(a). Firstly, we prepare NV center into a probe state $\frac{|0\rangle+|1\rangle}{\sqrt{2}}$. Then, the superposition state evolves under the unknown magnetic field $b(t)$ along the spin's quantization axis with a relative phase $\phi(t) = \int_0^t \gamma_e b(t) dt$, where γ_e is the gyromagnetic ratio of the spin. We can selectively acquire the phase from the time interval $[t_i, t_i + t_s]$ while canceling out unwanted dynamically phase evolution by inserting two π pulses at times t_i and $t_i + t_s$. For $t_s/T \ll 1$, we have $\phi(t_i) \approx -2\gamma_e b(t_i)t_s$ [37]. Finally, the accumulation phase is transferred into the initial phase of Rabi oscillation and measured with optical method. The protocol can be repeated k times to linearly increase the accumulation phase ($\phi_{n_2} = k\phi(t_i)$). Then, the number of resource used in TDQD protocol is $n_2 = 2k$ for each sampling. To suppress the quantum dephasing effect of ^{13}C nuclear spins in diamond [7], we exploit the PDD method by adding a time-delay of $2t_s$ after the waveform finishing, as shown in Fig. 2(a). In the present case, the quantum dynamic evolution of ^{13}C nuclear spins under the magnetic field $b(t)$ can be neglected ($\gamma_{^{13}\text{C}}bT_2 \ll 1$) and is approximately dominated by the static magnetic field and hyperfine field conditioned on the electron spin state [37, 45]. The PDD-enhanced TDQD protocol, which is $[t_i - \pi - (T + t_s) - \pi - (T - t_i + t_s)]^k$, consists of a sequence of π flips for the sensor evolution. By simply merging the free-evolution propagator term, it turns out to be $[t_i - PDD_{k-1} - \pi - (T + t_s) - \pi - (T - t_i + t_s)]$, where $PDD_{k-1} = [\pi - (T + t_s) - \pi - (T + t_s)]^{k-1}$. So the experimental signal is $s \sim \exp\left[-\left(\frac{2k(T+t_s)}{T_2}\right)^2\right] \cos \phi_{n_2}$ [37].

We first investigate the experimental result by accumulating phase from $n_2 = 2k$ consecutive waveform passages. Fig. 2(b) plots the readout of accumulation phase from a weak sinusoidal test signal recorded with different values of k . With the increase of k , a much stronger oscillation response is observed with a much higher dynamic range [25, 46]. Fig. 2(c) shows the readout process of an unknown accumulation phase with $k = 15$ and $t_i = 450$ ns. Furthermore, we explore the sensor signal as a function of k with a fixed $t_i = 450$ ns, as shown in Fig. 2(d). For a serial of k values, the accumulation phase is proportional to k . Without correcting the decoherence of NV center, we observe the exact linear scaling relationship. The overall sensitivity [25] in the

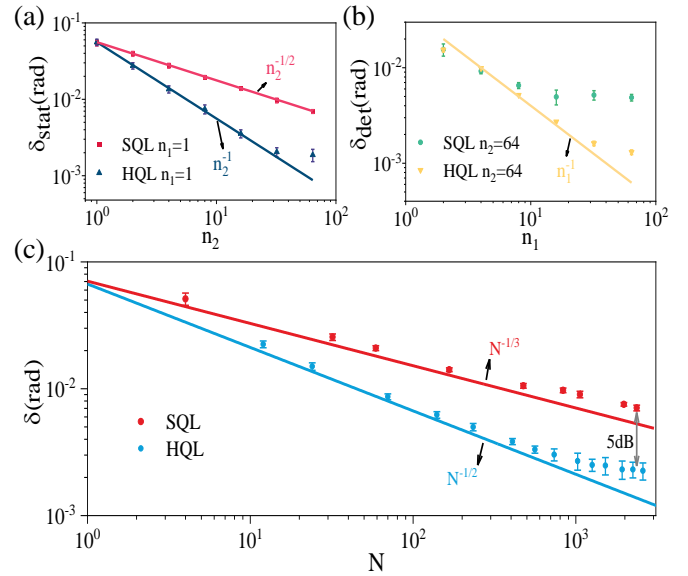


FIG. 3. SQL and HQL in waveform estimation. (a) The scaling laws (solid lines) $\delta_{stat} = O(n_2^{-1/2})$ for SQL and $\delta_{stat} = O(n_2^{-1})$ for HQL, respectively. (b) The deterministic error. The solid golden line shows $\delta_{det} = O(n_1^{-1})$. (c) Results of SQL and HQL in waveform estimation. The colored dots represent experimental results. The integration time is $t_s = \frac{T}{n_2}$ and $T = 9.6 \mu\text{s}$ is the period of the sinusoidal waveform.

presence of decoherence is also calculated and shown in Fig. 2(e). Obviously, the PDD-enhanced TDQD protocol extends dynamic range and improved the sensitivity of waveform estimation by one order of magnitude comparing with the normal TDQD protocol [25, 37]. Besides those advantages, the multi-pulse is also naturally immune to imperfect pulse error operation with phase modulation [47, 48].

To demonstrate the superiority of HQL in waveform estimation, we choose a 1st-order differentiable waveform in the experiment. And more importantly, the balance between δ_{stat} and δ_{det} should be optimized by tuning the width of smoothing (t_s). Here, we have an approximate relationship: $n_1 \sim n_2$ for large N , which indicates $\frac{T}{t_s + 2t_\pi} \sim \frac{T_2}{T}$ or $T \approx \sqrt{T_2}(t_s + 2t_\pi) \approx 10 \mu\text{s}$, where $T_2 = 0.66(2)$ ms [37] is the coherence time of NV center and T is the period of waveform. Here, we choose $T = 9.6 \mu\text{s}$ [37].

We test the basic scaling laws $\delta_{stat} = O(n_2^{-1/2})$ for the SQL with small-interval Ramsey sensing sequence [25, 37] and $\delta_{stat} = O(n_2^{-1})$ for the HQL in the estimation of a sinusoidal waveform. The experimental results are shown in Fig. 3(a), together with theoretical calculations. The sensitivity of the unknown accumulation phase is therefore increased by $\sqrt{n_2}$ -fold compared with uncorrelated quantum resource, yielding the Heisenberg scaling. Results in Fig. 3(a) also show that as the number of quantum resources further increases when $n \geq 64$, δ_{stat} starts to gradually deviate from theoretical values of HQL. This

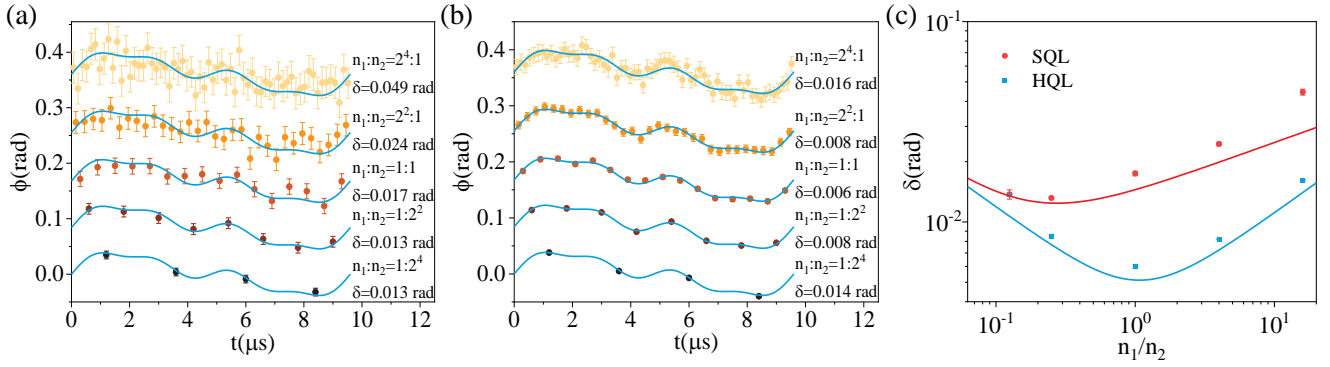


FIG. 4. An example of waveform detection with PDD-enhanced TDQD protocol. (a) Results of the SQL scheme. (b) Results of the HQL scheme. The total number of resources is $N = 2^8$. The experimental results are shown in stack graph by Y offsets. The input waveform (solid blue line) and the recorded waveform data (colored dots) are given by $b(t) = b[\sin(2\pi t/T) + 0.5\sin(4\pi t/T) + 0.25\sin(8\pi t/T)]$ with $T = 9.6 \mu s$. (c) Waveform estimation errors (colored dots) with different resource distributions. When the balance between these two errors is broken, the overall waveform estimation errors increase [37].

is caused by the decoherence effects ($T_2 \sim 64T$) of the NV center [37]. However, for the SQL scheme, we can neglect this decoherence effect. Furthermore, the results of δ_{det} are shown in Fig. 3(b). There is an apparent contradiction between experimental and theoretical results for the SQL scheme because δ_{stat} is quite large. In this case, noise in waveform reconstruction greatly increases due to the imperfection convergency of experimental data and the relationship $\delta_{det} = O(n_1^{-1})$ will be overwhelmed by noise. However, this type of error is reduced by employing HQL scheme and the basic scaling laws $\delta_{det} = O(n_1^{-1})$ emerges. When δ_{stat} deviates from the theoretical prediction under decoherence, δ_{det} will also deviate from $O(n_1^{-1})$. So these two kinds of estimation errors are tangled up in the experiment for the waveform reconstruction. By making use of the inequality of arithmetic and geometric means, the trade-off between δ_{stat} and δ_{det} can be optimized numerically [37]. Fig. 3(c) shows this key experimental results of overall waveform estimation errors. For the 1st-order differentiable waveform estimation, the fundamental limits bounded by $\delta = O(N^{-1/3})$ for SQL and $\delta = O(N^{-1/2})$ for HQL are experimentally demonstrated. The HQL-scaled waveform estimation based on the PDD-enhanced TDQD protocol clearly demonstrates the superiority of quantum metrology. For example, we have demonstrated the use of $\sim 2 \times 10^3$ resources to achieve the waveform estimation error 5 dB below the SQL. While more than 1×10^5 resources would be required to achieve a similar error level using standard classical techniques.

We further complete our study by demonstrating the reconstruction of a complex test waveform, which contains the sum of several frequency components. The experimentally measured waveform in SQL and HQL scheme together with the input waveform are shown in Fig. 4(a) and (b), respectively. With the same num-

ber of resources, the superiority of HQL scheme for waveform estimation is observed clearly in the experiment. By employing quantum correlation with the PDD-enhanced TDQD protocol, the statistical error is reduced and the measurement results converge to the ideal value quickly. Clearly, the overall waveform estimation error δ is changed with the proportion of resource distribution. For a given number of resource $N = n_1 n_2$, the optimal accuracy is determined by the trade-off between δ_{stat} and δ_{det} , as shown in Fig. 4(c). When $n_1 \sim n_2$, the optimal waveform reconstruction of $q = 1$ is realized in HQL scheme with NV center. A similar relationship also applies to the SQL case [37].

In summary, we present a PDD-enhanced TDQD protocol for Heisenberg-limited arbitrary reproducible waveform estimation. The current results demonstrate the potential of the quantum measurement technique, which is readily available for other quantum probe systems [4, 49, 50]. For the 1st-order differentiable arbitrary waveform, we demonstrate the SQL of $O(N^{-1/3})$ and the HQL of $O(N^{-1/2})$ in the experiment, which is significantly different with previous parametric estimation. This new fundamental result sets a new quantum-enhanced metrology scaling law of high precision detection of continuous physical signals [22–24]. And far more than physical scope, the estimation of continuous signals and images in micro-fluidic chemical analysis [51], vital activity [26, 52] and pattern recognition [53] in computer science would be significantly improved by making use of the quantum superiority. Moreover, the waveform sampling based on the TDQD protocol will benchmark the quantum version of the Nyquist-Shannon sampling theorem [23], which would directly knock on the door of the practical quantum oscilloscope.

Beyond the current work, multiple entangled state [4, 13, 18, 19] can be applied to achieve same quantum-

enhanced waveform estimation with parallel schemes. And more general unpredictable signal can be detected at one time. For the TDQD and parallel schemes, same quantum coherent amplification of unknown phase can be realized and the detection resolution can reach the Heisenberg-limited scaling. That is the quantum Cramér-Rao bound can be asymptotically approached in both cases. Here, the equivalence between entanglement in parallel schemes and coherence (namely, superposition in the eigenbasis of the generator) can be understood by observing that both nonclassicality in infinite-dimensional systems and coherence (superposition) in finite-dimensional systems can be converted to entanglement within a well-defined resource-theoretic framework [3, 11]. This precise understanding and control of genuine quantum effects such as nonclassicality and superposition will further extend the application of quantum metrology in the future.

This work is supported by the National Key Research and Development Program of China (Grant No. 2017YFA0304504), the National Natural Science Foundation of China (Grants No. 91536219, No. 61522508, and No. 91850102), the Anhui Initiative in Quantum Information Technologies (Grant No. AHY130000), the Science Challenge Project (Grant No. TZ2018003), and the Fundamental Research Funds for the Central Universities (No. WK2030000020).

* fwsun@ustc.edu.cn

- [1] V. Giovannetti, S. Lloyd, and L. Maccone, *Nat. Photonics* **5**, 222 (2011).
- [2] L. Pezzè, A. Smerzi, M. K. Oberthaler, R. Schmied, and P. Treutlein, *Rev. Mod. Phys.* **90**, 035005 (2018).
- [3] D. Braun, G. Adesso, F. Benatti, R. Floreanini, U. Marzolino, M. W. Mitchell, and S. Pirandola, *Rev. Mod. Phys.* **90**, 035006 (2018).
- [4] S. Pirandola, B. R. Bardhan, T. Gehring, C. Weedbrook, and S. Lloyd, *Nat. Photonics* **12**, 724 (2018).
- [5] F. W. Sun, B. H. Liu, Y. X. Gong, Y. F. Huang, Z. Y. Ou, and G. C. Guo, *EPL* **82**, 24001 (2008).
- [6] B. L. Higgins, D. W. Berry, S. D. Bartlett, H. M. Wiseman, and G. J. Pryde, *Nature* **450**, 393 (2007).
- [7] Y. Dong, X.-D. Chen, G.-C. Guo, and F.-W. Sun, *Phys. Rev. A* **94**, 052322 (2016).
- [8] E. M. Kessler, I. Lovchinsky, A. O. Sushkov, and M. D. Lukin, *Phys. Rev. Lett.* **112** (2014).
- [9] A. Streltsov, G. Adesso, and M. B. Plenio, *Rev. Mod. Phys.* **89**, 041003 (2017).
- [10] Y. Dong, Y. Zheng, S. Li, C.-C. Li, X.-D. Chen, G.-C. Guo, and F.-W. Sun, *npj Quantum Inf.* **4**, 3 (2018).
- [11] T. Nishioka, *Rev. Mod. Phys.* **90**, 035007 (2018).
- [12] Y. Dong, X.-D. Chen, G.-C. Guo, and F.-W. Sun, *Phys. Rev. B* **100**, 214103 (2019).
- [13] B. Han, J. Duan, S. Jin, X. Lu, P. Li, W. Qu, M. Wang, N. Irina, E. E. Mikhailov, Z. Kai-Feng, et al., *Nature* **581**, 159 (2020).
- [14] J.-W. Pan, Z.-B. Chen, C.-Y. Lu, H. Weinfurter, A. Zeilinger, and M. Żukowski, *Rev. Mod. Phys.* **84**, 777 (2012).
- [15] Z. Hou, R.-J. Wang, J.-F. Tang, H. Yuan, G.-Y. Xiang, C.-F. Li, and G.-C. Guo, *Phys. Rev. Lett.* **123**, 040501 (2019).
- [16] K. R. Motes, J. P. Olson, E. J. Rabeaux, J. P. Dowling, S. J. Olson, and P. P. Rohde, *Phys. Rev. Lett.* **114**, 170802 (2015).
- [17] T. Monz, P. Schindler, J. T. Barreiro, M. Chwalla, D. Nigg, W. A. Coish, M. Harlander, W. Hänsel, M. Hennrich, and R. Blatt, *Phys. Rev. Lett.* **106**, 130506 (2011).
- [18] A. Omran, H. Levine, A. Keesling, G. Semeghini, T. T. Wang, S. Ebadi, H. Bernien, A. S. Zibrov, H. Pichler, S. Choi, et al., *Science* **365**, 570 (2019).
- [19] C. Song, K. Xu, H. Li, Y.-R. Zhang, X. Zhang, W. Liu, Q. Guo, Z. Wang, W. Ren, J. Hao, et al., *Science* **365**, 574 (2019).
- [20] C. E. Bradley, J. Randall, M. H. Abobeih, R. C. Berrevoets, M. J. Degen, M. A. Bakker, M. Markham, D. J. Twitchen, and T. H. Taminiau, *Phys. Rev. X* **9**, 031045 (2019).
- [21] G.-Q. Liu, Y.-R. Zhang, Y.-C. Chang, J.-D. Yue, H. Fan, and X.-Y. Pan, *Nat. Commun.* **6**, 6726 (2015).
- [22] J. Abadie, B. Abbott, R. Abbott, T. D. Abbott, M. R. Abernathy, C. Adams, R. X. Adhikari, C. Affeldt, B. Allen, G. S. Allen, et al., *Nat. Phys.* **7**, 962 (2011).
- [23] N. Kura and M. Ueda, *Phys. Rev. Lett.* **124**, 010507 (2020).
- [24] A. Cooper, E. Magesan, H. N. Yum, and P. Cappellaro, *Nat. Commun.* **5**, 3141 (2014).
- [25] J. Zopes and C. Degen, *Phys. Rev. Appl.* **12**, 054028 (2019).
- [26] X. Michalet, F. Pinaud, L. Bentolila, J. Tsay, S. Doose, J. Li, G. Sundaresan, A. Wu, S. Gambhir, and S. Weiss, *Science* **307**, 538 (2005).
- [27] D. Budker and M. Romalis, *Nat. Phys.* **3**, 227 (2007).
- [28] G. Brida, M. Genovese, and I. R. Berchera, *Nat. Photonics* **4**, 227 (2010).
- [29] N. Samantaray, I. Ruo-Berchera, A. Meda, and M. Genovese, *Light Sci. Appl.* **6**, e17005 (2017).
- [30] K. Akiyama, A. Alberdi, W. Alef, K. Asada, R. Azulay, A.-K. Baczkó, D. Ball, M. Baloković, J. Barrett, D. Bintley, et al., *Astrophys. J.* **875**, L3 (2019).
- [31] K. Akiyama, A. Alberdi, W. Alef, K. Asada, R. Azulay, A.-K. Baczkó, D. Ball, M. Baloković, J. Barrett, D. Bintley, et al., *Astrophys. J.* **875**, L4 (2019).
- [32] G. Chen, L. Zhang, W.-H. Zhang, X.-X. Peng, L. Xu, Z.-D. Liu, X.-Y. Xu, J.-S. Tang, Y.-N. Sun, D.-Y. He, et al., *Phys. Rev. Lett.* **121**, 060506 (2018).
- [33] M. Kitagawa and M. Ueda, *Phys. Rev. A* **47**, 5138 (1993).
- [34] Y.-C. Zhang, X.-F. Zhou, X. Zhou, G.-C. Guo, and Z.-W. Zhou, *Phys. Rev. Lett.* **118**, 083604 (2017).
- [35] M. C. Kuzyk and H. Wang, *Phys. Rev. X* **8**, 041027 (2018).
- [36] A. V. Oppenheim, A. S. Willsky, and S. Hamid, *Signals and Systems* (Prentice Hall, Englewood Cliffs, NJ, 1997).
- [37] See Supplemental Material at [] for the calculation of estimation error of waveform, introduction to the NV center, experimental setup, TDQD and PDD-enhanced TDQD protocol, and the optimal resource allocation of SQL and HQL schemes, which includes Refs. [38-40].
- [38] A. M. Souza, G. A. Álvarez, and D. Suter, *Phys. Rev. Lett.* **106**, 240501 (2011).

-
- [39] E. D. Herbschleb, H. Kato, Y. Maruyama, T. Danjo, T. Makino, S. Yamasaki, I. Ohki, K. Hayashi, H. Morishita, M. Fujiwara, et al., *Nat. Commun.* **10**, 3766 (2019).
- [40] J. Nocedal and S. J. Wright, *Numerical Optimization* (Springer, New York, 2006).
- [41] J. F. Barry, J. M. Schloss, E. Bauch, M. J. Turner, C. A. Hart, L. M. Pham, and R. L. Walsworth, *Rev. Mod. Phys.* **92**, 015004 (2020).
- [42] H. Clevenston, M. E. Trusheim, C. Teale, T. Schroeder, D. Braje, and D. Englund, *Nat. Phys.* **11**, 393 (2015).
- [43] X.-D. Chen, D.-F. Li, Y. Zheng, S. Li, B. Du, Y. Dong, C.-H. Dong, G.-C. Guo, and F.-W. Sun, *Phys. Rev. Appl.* **12**, 044039 (2019).
- [44] Y. Dong, S.-C. Zhang, H.-B. Lin, X.-D. Chen, W. Zhu, G.-Z. Wang, G.-C. Guo, and F.-W. Sun, [arXiv:2003.02472](https://arxiv.org/abs/2003.02472) (2020).
- [45] N. Zhao, S.-W. Ho, and R.-B. Liu, *Phys. Rev. B* **85**, 115303 (2012).
- [46] K. Arai, J. Lee, C. Belthangady, D. R. Glenn, H. Zhang, and R. L. Walsworth, *Nat. Commun.* **9**, 4996 (2018).
- [47] G. T. Genov, D. Schraft, N. V. Vitanov, and T. Halfmann, *Phys. Rev. Lett.* **118**, 133202 (2017).
- [48] Z.-Y. Wang, J. E. Lang, S. Schmitt, J. Lang, J. Casanova, L. McGuinness, T. S. Monteiro, F. Jelezko, and M. B. Plenio, *Phys. Rev. Lett.* **122** (2019).
- [49] C. L. Degen, F. Reinhard, and P. Cappellaro, *Rev. Mod. Phys.* **89**, 035002 (2017).
- [50] M. W. Mitchell and S. Palacios Alvarez, *Rev. Mod. Phys.* **92**, 021001 (2020).
- [51] K. Lim, C. Ropp, B. Shapiro, J. M. Taylor, and E. Waks, *Nano Lett.* **15**, 1481 (2015).
- [52] J. F. Barry, M. J. Turner, J. M. Schloss, D. R. Glenn, Y. Song, M. D. Lukin, H. Park, and R. L. Walsworth, *Proc. Natl. Acad. Sci.* **113**, 14133 (2016).
- [53] Z. Wang, S. Joshi, S. Savel'ev, W. Song, R. Midya, Y. Li, M. Rao, P. Yan, S. Asapu, Y. Zhuo, et al., *Nat. Electron.* **1**, 137 (2018).

Supplemental Material: Heisenberg-Limited Waveform Estimation with Solid-State Spins in Diamond

Yang Dong,^{1,2} Ze-Hao Wang,^{1,2} Hao-Bin Lin,^{1,2} Shao-Chun Zhang,^{1,2} Yu Zheng,^{1,2} Xiang-Dong Chen,³ Wei Zhu,³ Guan-Zhong Wang,³ Guang-Can Guo,^{1,2} and Fang-Wen Sun^{1,2,*}

¹*CAS Key Laboratory of Quantum Information,*

University of Science and Technology of China, Hefei, 230026, P.R. China

²*CAS Center for Excellence in Quantum Information and Quantum Physics,*

University of Science and Technology of China, Hefei, 230026, P.R. China

³*Hefei National Laboratory for Physical Science at Microscale, and Department of Physics,*

University of Science and Technology of China, Hefei, Anhui 230026, P. R. China

I. THE ESTIMATION ERROR OF WAVEFORM BASED ON THE LEAST SQUARE METHOD

With the standard measurement scheme, we estimate the unknown waveform based on $N = n_1 n_2$ measurement results. In the present case, the overall results can be divided into n_1 equal parts according to sampling time. For the sampling instant t_i , we have a serial outputs $\{\phi_{i,j}\}$ to get the unknown phase, where $i = 1, 2, \dots, n_1$ and $j = 1, 2, \dots, n_2$. Hence, the total estimation error of waveform have a simple form:

$$\begin{aligned}
 \delta^2 &= \mathbb{E} \left[\int_0^T \frac{dt}{T} [\tilde{\phi}(t) - \phi(t)]^2 \right] \\
 &= \frac{1}{n_2} \sum_{j=1}^{n_2} \left[\int_0^T \frac{dt}{T} \left(\sum_{i=1}^{n_1} \phi_{i,j} \theta(t - t_i) - \phi(t) \right)^2 \right] \\
 &= \frac{1}{n_2} \sum_{j=1}^{n_2} \sum_{i=1}^{n_1} \int_{t_i - \frac{T}{2n_1}}^{t_i + \frac{T}{2n_1}} \frac{dt}{T} [\phi_{i,j} - \phi(t)]^2 \\
 &= \sum_{i=1}^{n_1} \left[\frac{1}{n_2} \sum_{j=1}^{n_2} \int_{t_i - \frac{T}{2n_1}}^{t_i + \frac{T}{2n_1}} \frac{dt}{T} [\phi_{i,j} - \bar{\phi}_i + \bar{\phi}_i - \phi(t)]^2 \right],
 \end{aligned} \tag{S1}$$

*Electronic address: fwsun@ustc.edu.cn

where we define $\bar{\phi}_i = \frac{1}{n_2} \sum_{j=1}^{n_2} \phi_{i,j}$ based on the least square method. In this way, the cross-term is zero:

$$\sum_{i=1}^{n_1} \left[\frac{1}{n_2} \sum_{j=1}^{n_2} \int_{t_i - \frac{T}{2n_1}}^{t_i + \frac{T}{2n_1}} \frac{dt}{T} 2(\phi_{i,j} - \bar{\phi}_i)(\bar{\phi}_i - \phi(t)) \right] = 0.$$

And we have

$$\begin{aligned} \delta^2 &= \sum_{i=1}^{n_1} \left[\frac{1}{n_2} \sum_{j=1}^{n_2} \int_{t_i - \frac{T}{2n_1}}^{t_i + \frac{T}{2n_1}} \frac{dt}{T} (\phi_{i,j} - \bar{\phi}_i)^2 + \frac{1}{n_2} \sum_{j=1}^{n_2} \int_{t_i - \frac{T}{2n_1}}^{t_i + \frac{T}{2n_1}} \frac{dt}{T} (\bar{\phi}_i - \phi(t))^2 \right] \\ &= \sum_{i=1}^{n_1} \left[\int_{t_i - \frac{T}{2n_1}}^{t_i + \frac{T}{2n_1}} \frac{dt}{T} \delta_{i,stat}^2 + \int_{t_i - \frac{T}{2n_1}}^{t_i + \frac{T}{2n_1}} \frac{dt}{T} \delta_{i,det}^2 \right] \\ &= \frac{1}{n_1} \sum_{i=1}^{n_1} \delta_{i,stat}^2 + \sum_{i=1}^{n_1} \int_{t_i - \frac{T}{2n_1}}^{t_i + \frac{T}{2n_1}} \frac{dt}{T} \delta_{i,det}^2 \\ &= \frac{1}{n_1} \sum_{i=1}^{n_1} \delta_{i,stat}^2 + \int_0^T \frac{dt}{T} \delta_{i,det}^2 \\ &= \delta_{stat}^2 + \delta_{det}^2, \end{aligned} \tag{S2}$$

where $\delta_{i,stat}^2 = \frac{1}{n_2} \sum_{j=1}^{n_2} (\phi_{i,j} - \bar{\phi}_i)^2$ and $\delta_{i,det}^2 = (\bar{\phi}_i \theta(t - t_i) - \phi(t))^2$.

So the overall arbitrary waveform estimation error can be decomposed into two parts: the statistical error $\delta_{stat}^2 = \frac{1}{n_1} \sum_{i=1}^{n_1} \delta_{i,stat}^2$ caused by the projection measurement and the deterministic error $\delta_{det}^2 = \int_0^T \frac{dt}{T} \delta_{i,det}^2$ due to the smoothing process as shown in the main text. As n_2 increases large enough, the average measurement result $\bar{\phi}_i$ would converge to the ideal value due to the central limit theorem. And for a finite number of experiment repeats, there will be some of the discrepancy between theory and experiment. Under the restrictions of $\sup_{0 < \varepsilon < a} \int_0^T \frac{dt}{T} \left| \frac{\phi(t+\varepsilon) - \phi(t)}{\varepsilon^q} \right|^2 \leq \frac{M^2}{T^{2q}}$ for some positive number $M > 0$ [1], we have the Hölder continuity $|\phi(t + \varepsilon) - \phi(t)| = O(\varepsilon^q)$ equivalently. So once the average measurement results $\bar{\phi}_i$ converges to the ideal values of arbitrary waveform, the deterministic error scales as

$$\begin{aligned} \delta_{det}^2 &= \sum_{i=1}^{n_1} \int_{t_i - \frac{T}{2n_1}}^{t_i + \frac{T}{2n_1}} \frac{dt}{T} (\bar{\phi}_i \theta(t - t_i) - \phi(t))^2 \\ &= \sum_{i=1}^{n_1} \int_{-\frac{T}{2n_1}}^{\frac{T}{2n_1}} \frac{dt}{T} O(t^{2q}) \\ &= O(n_1^{-2q}). \end{aligned} \tag{S3}$$

For a given number of resources $N = n_1 n_2$, the optimal measurement is determined by the trade-off between these errors. By employing the inequality of arithmetic and geometric means, the estimation error of arbitrary waveform is

$$\begin{aligned} \delta^2 &= \delta_{det}^2 + \delta_{stat}^2 \\ &= O(M n_1^{-2q}) + O(n_2^{-1}) \\ &\geq O\left(\left(M^{1/q} N^{-1}\right)^{2q/(2q+1)}\right) \end{aligned} \tag{S4}$$

in SQL scheme. If we neglect the constant factor, we will get the optimal scaling relationship $\delta = O(N^{-q/(2q+1)})$ in the SQL scheme. With similar procedure, the total estimation error would be reduced with correlative quantum resources and scale as $\delta = O(N^{-q/(q+1)})$ in the HQL scheme. The optimal quantum resource allocation of arbitrary waveform estimation would meet this condition $n_1^{-2q} \sim n_2^{-1}$ for SQL and $n_1^{-2q} \sim n_2^{-2}$ for HQL with large N . And this relationship has a simple form: $\log_2 n_1 = \frac{1}{2q} \log_2 n_2 + c_1$ and $\log_2 n_1 = \frac{1}{q} \log_2 n_2 + c_2$ for SQL and HQL, respectively.

II. NV CENTER IN DIAMOND

The negatively charged NV center in diamond, where a substitutional nitrogen atom is next to a vacancy, forms a spin triplet system in its ground state as shown in Fig. S1(a). Conveniently, the NV spin can be initialized using optical pumping under green laser excitation and optically read out by its spin-dependent fluorescence with a home-built confocal microscopy at room-temperature. The NV's spin sub-levels of ground state are $|0\rangle$ and $|\pm 1\rangle$. The zero-field splitting between $|0\rangle$ and degenerate $|\pm 1\rangle$ sub-levels is $D = 2.87$ GHz. In the experiment, we apply a strength of the external magnetic field near the excited state level anti-crossing [2], i.e., $B_0 \approx 38$ mT along the NV symmetry axis to split the energy levels and polarize intrinsic ^{14}N nuclear spin to enhance the signal contrast up to $C = 0.25$.

We use a room-temperature home-built confocal microscopy, with a dry objective lens (N.A. = 0.95 Olympus), to image, initialize and read out NV center in a single-crystal synthetic diamond sample. The NV centers studied in this work are formed during chemical vapour deposition growth. The abundance of ^{13}C was at the nature level of 1%. Single NV centers are identified by observing anti-bunching in photon correlation measurements and

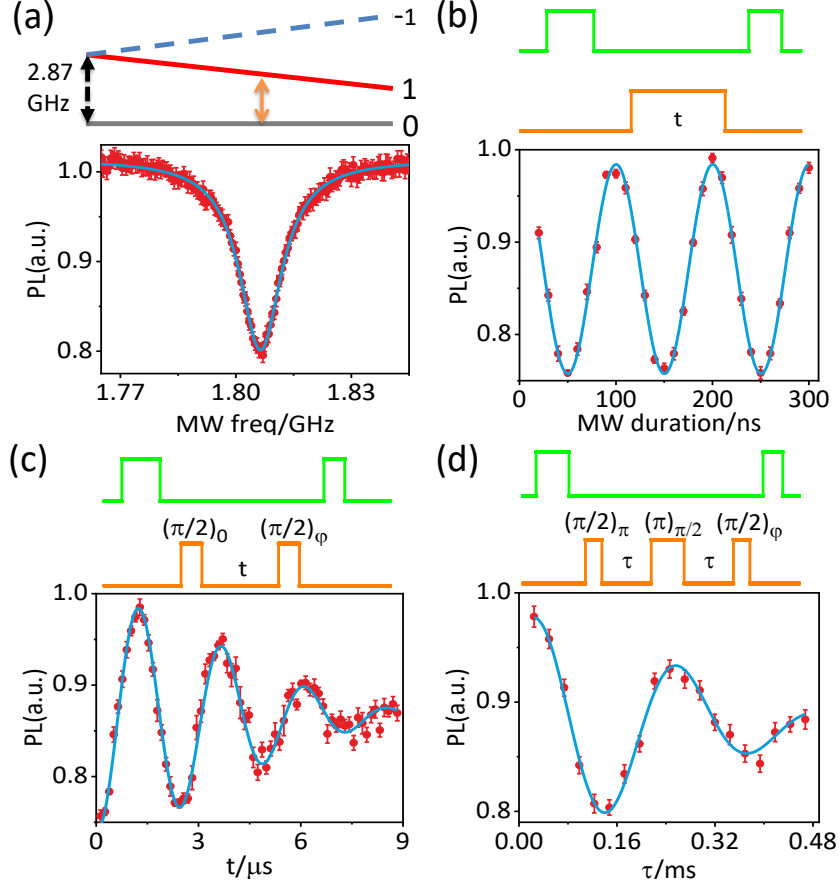


FIG. S1: (a) Energy-level diagram of the NV center under external magnetic field B_0 (upper panel) and the pulsed-ODMR spectrum of $|0\rangle \leftrightarrow |1\rangle$ with $B_0 \approx 38$ mT (lower panel). The transition frequencies for $|0\rangle \leftrightarrow |1\rangle$ is 1.806 GHz. (b) Results of the nutation experiment for the electron spin and Rabi frequency is $\Omega = 10$ MHz. (c) FID of the electron spin with an dephasing time $T_2^* = 5.2(1)$ μs . (d) Spin echo pulse sequence used for coherence time measurement with $T_2 = 0.66(2)$ ms.

the measurement of the spin splitting at zero magnetic field. The NV center is mounted on a three-axis closed-loop piezoelectric stage for sub-micrometre-resolution scanning. Fluorescence photons (wavelength ranging from 647 to 800 nm) are collected into a fiber and detected using single-photon counting module, with a counting rate of 50 kHz and a signal-to-noise ratio of 50 : 1. A copper wire of 10 μm diameter above on the bulk diamond is used for the delivery of MW and arbitrary waveform to the NV center. The driving MW is generated by an AWG (Keysight M8190a) and amplified by a microwave amplifier (Mini-circuits ZHL-5W-2G-S+). The optical and MW pulse sequences are synchronized by a multichannel pulse generator (Spincore, PBESR-PRO-500).

Electron spin states $|0\rangle$ and $|1\rangle$ of NV center are encoded as the sensor qubit. Under resonance condition, the Rabi frequency is set to be $\Omega = 10$ MHz in experiment, as shown in

Fig. S1(b). The undesired couplings between the NV center and the surrounding ^{13}C nuclear spins lead to the effective dephasing effect. The resulting free induction decay (FID) of the NV center is depicted in Fig. S1(c), where a dephasing time $T_2^* = 5.2(1) \mu\text{s}$ is obtained. The coherence times $T_2 = 0.66(2) \text{ ms}$ is observed, as shown in Fig. S1(d).

III. QUANTUM SENSING OF ARBITRARY WAVEFORMS

The time-domain quantum difference (TDQD) protocol follows a general sequence of sensor initialization, interaction with the waveform, sensor readout, and signal estimation. This sequence can be summarized in the following basic protocol:

Step 1: The quantum sensor is initialized into a known ground state, for example, $|0\rangle$.

Step 2: The quantum sensor is transformed into the desired initial sensing state $|\psi\rangle = \frac{|0\rangle + |1\rangle}{\sqrt{2}}$ with a $\frac{\pi}{2}$ pulse.

Step 3: The superposition state evolves under the magnetic field $b(t)$ that we aim to measure at a time t_i . The superposition state picks up the relative phase:

$$\phi(t_i) = \int_0^{t_i} \gamma_e b(t) dt - \int_{t_i}^T \gamma_e b(t) dt - \int_0^{t_i+t_s} \gamma_e b(t) dt + \int_{t_i+t_s}^T \gamma_e b(t) dt = -2 \int_{t_i}^{t_i+t_s} \gamma_e b(t) dt.$$

For $t_s/T \ll 1$, we have $\phi(t_i) \approx -2\gamma_e b(t_i)t_s$.

Step 4: Using a second $\frac{\pi}{2}$ pulse, the relative phase is mapped into x-y plane of Bloch sphere.

Step 5: The final state of the quantum sensor is read out by employing the initial phase of Rabi oscillation.

Steps 1–5 represent a single measurement cycle. To reduce the fluctuation of detection signal, the measurement cycle needs to be repeated many times (2×10^6) in experiment. And we can control the repetition times (k) of Step 3 to linearly increase the accumulation relative phase ($\phi_{n_2} = k\phi(t_i)$). The number of resources used in TDQD protocol is $n_2 = 2k$ for each sampling. The whole pulse sequences are shown in Fig. S2(a) based on NV center sensor in diamond. Fig. S2(b) shows the basic dynamic evolution of quantum sensor qubit with a Bloch sphere. The sensor outputs $s(t)$ for a serial of k values of the two- π -pulse unit

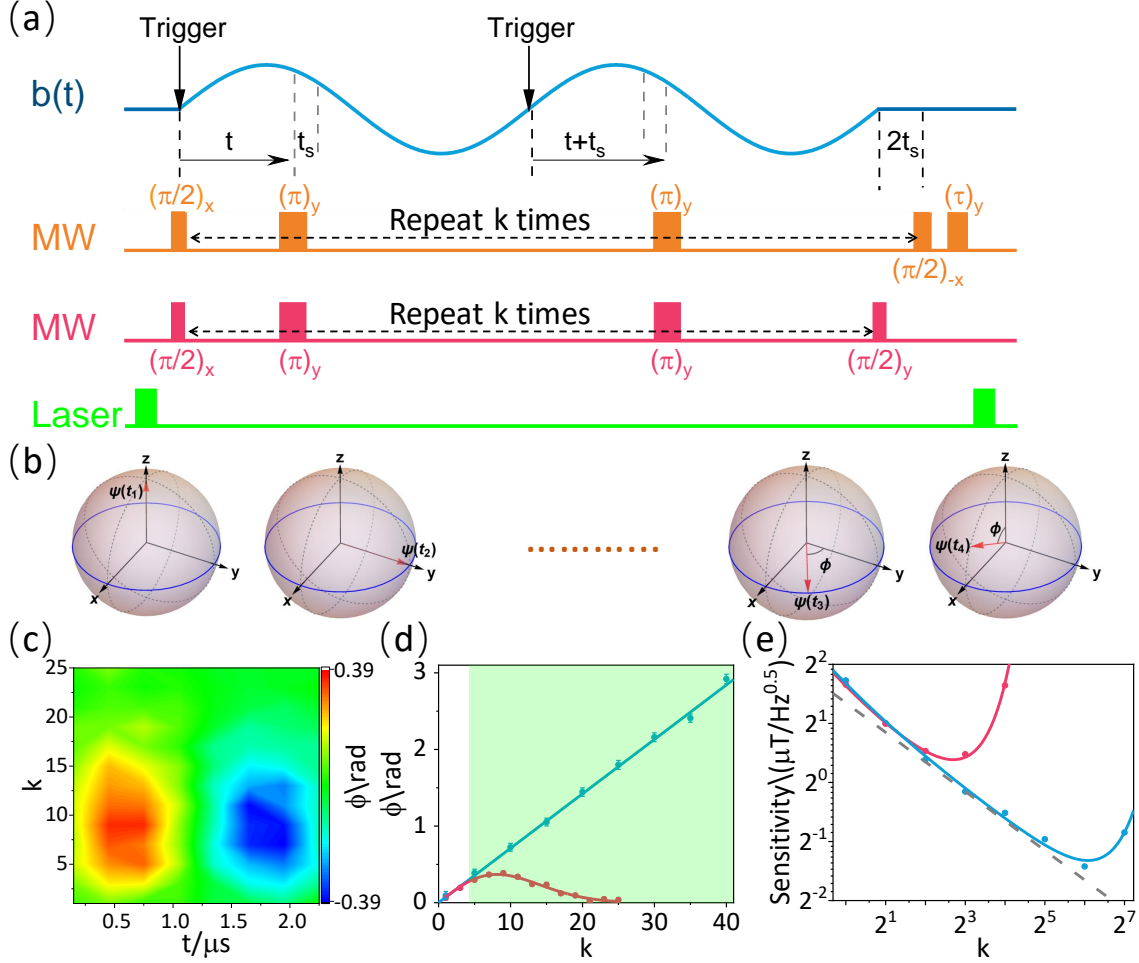


FIG. S2: (a) Pulse sequence for waveform sampling. Based on PDD, we propose the robust TDQD detection method (orange pulse train). By scanning the moment of applying π gates, the arbitrary waveform can be reconstructed. As a comparison, the original TDQD protocol is plotted with pink. (b) Dynamically process of TDQD protocol with Bloch sphere. (c) Increased sensitivity by integrating $2k$ waveform passages with the differential spin-echo detection. (d-e) Comparison of two arbitrary waveform estimation protocols. Red (blue) lines and dots show the theoretical and experimental results with (PDD-enhanced) TDQD protocol.

in the estimation of a sinusoidal waveform with period of $T = 2.4 \mu\text{s}$. The integration time and π -pulse duration are $t_s = 300 \text{ ns}$ and $t_\pi = 50 \text{ ns}$, respectively.

In the original protocol of reconstruction-free quantum sensing of arbitrary waveforms [3], the only idea of unwanted dynamic evolution coherent cancellation is exploited with two- π -pulse block as shown in Fig. S2(a) with pink pulse train. The signal of the waveform

sampling at t_i can be expressed as:

$$s \sim \exp \left[-\left(\frac{2kt_s}{T_2^*} \right)^2 \right] \exp \left[-\left(\frac{2kT}{T_2} \right)^2 \right] \sin 2k\phi_i. \quad (\text{S5})$$

For small value k , $s \sim \exp \left[-\left(\frac{2kt_s}{T_2^*} \right)^2 \right] \exp \left[-\left(\frac{2kT}{T_2} \right)^2 \right] 2k\phi_i$ [3]. Due to dephasing effect and simple accumulation phase readout method, the sensitivity ($4 \mu T / \sqrt{Hz}$) and dynamic range ($[0, 0.05]$ rad) of reconstruction waveform is limited seriously based on the original TDQD protocol [3] in practice. We repeat the TDQD protocol, and the results are shown in Fig. S2(c). Clearly, with the increasing value of k , the TDQD method would be invalid in experiment.

In this work, we directly improve the differential-waveform sampling with periodic dynamical decoupling (PDD) method [4], which is a powerful technique for protecting qubits in quantum computing and quantum memory from the environment. The decay time constant of signal can be directly obtained and the signal for our protocol is

$$s \sim \exp \left[-\left(\frac{2k(T + t_s)}{T_2} \right)^2 \right] \cos 2k\phi_i. \quad (\text{S6})$$

So the PDD-enhanced TDQD protocol can coherently amplify accumulation phase, cancel unwanted coherent dynamical evolution and suppress quantum decoherence simultaneously. Beside those advantages, the PDD-enhanced TDQD is also immune to imperfect pulse error operation. The green shadow region in Fig. S2(d) denotes the dynamic range improvement

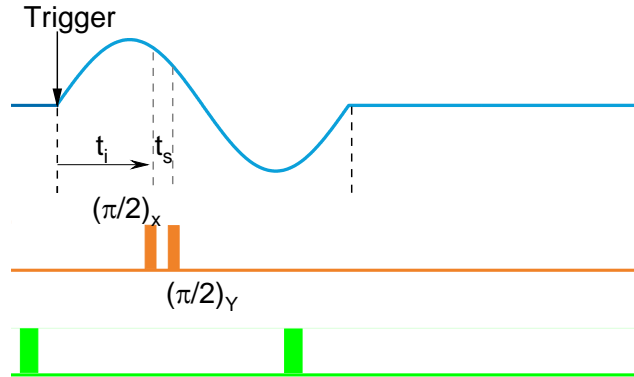


FIG. S3: Pulse sequence for the SQL measurement of waveform sampling. This sensor sequence was repeated for given numbers as shown in Fig. 3(a) of main text.

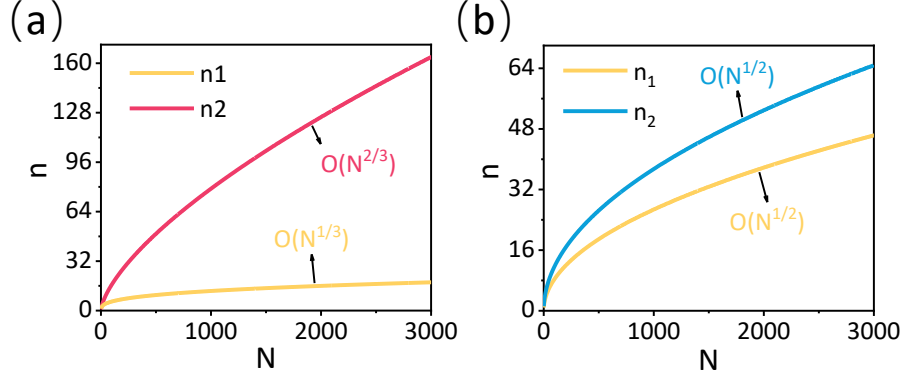


FIG. S4: (a)(b) The best allocation of quantum resource for waveform estimation with SQL or HQL scheme, respectively.

of the PDD-enhanced TDQD protocol. To quantify the sensitivity in the presence of decoherence and sensor readout overhead, we calculate a minimum detectable field B_{min} [3], defined as the input waveform that gives a unity signal-to-noise ratio for a given integration time, as shown in Fig. S2(e). To suppress the pure dephasing effect of ^{13}C further, the period of unknown arbitrary waveform should satisfy $\gamma_{^{13}\text{C}}B_0T \approx 2m\pi$ for NV center in diamond, where m is a positive integer number. Assisting with ^{12}C -enriched growth technology [5], this constraint condition can be totally dropped.

For the SQL in arbitrary waveform estimation, the small-interval ramsey detection is employed to avoid numerical processing as shown in Fig. S3. To perfectly demonstrate the advantage of HQL in arbitrary waveform estimation with our current technology, we chose a 1th-order differentiable waveform in experiment. And the period of waveform approximately satisfies $\gamma_{^{13}\text{C}}B_0T \approx 8\pi$, where $T = 9.6 \mu\text{s}$. The maximal number of samples in one period is $n_1 = \frac{T}{t_s + 2t_\pi} \sim 64$, where $t_s = 150 \text{ ns}$. So, the multi-round number is $n_2 = \frac{T}{T_2} \approx n_1$. By fitting experimental results in Fig.3(a) in the main text, the scaling laws show $\delta_{stat} = 0.0555/\sqrt{n_2}$ ($\delta_{stat} = 0.0555/n_2$) for SQL (HQL) and $\delta_{det} = 0.04/n_1$. Since the overall error is $\delta^2 = \delta_{det}^2 + \delta_{stat}^2$, the best allocation of quantum resource for the waveform estimation can be calculated with numerical method and results are shown in Fig. S4(a) and (b). In experiment, we exploit numerical approximate rounding method [6] to get the best quantum resource allocation approximately as shown in Tables I–II and Fig. 3(b) in the main text.

[1] N. Kura and M. Ueda, Phys. Rev. Lett. **124**, 010507 (2020).

TABLE I: Optimal resource allocation of SQL scheme.

| NO. | 1 | 2 | 3 | 4 | 5 | 6 | 7 | 8 | 9 |
|-------|---|----|----|-----|-----|-----|------|------|------|
| N | 4 | 32 | 60 | 168 | 480 | 840 | 1066 | 1984 | 2380 |
| n_1 | 2 | 4 | 5 | 7 | 10 | 12 | 13 | 16 | 17 |
| n_2 | 2 | 8 | 12 | 24 | 48 | 70 | 82 | 124 | 140 |

TABLE II: Optimal resource allocation of HQL scheme.

| NO. | 1 | 2 | 3 | 4 | 5 | 6 | 7 | 8 | 9 | 10 | 11 | 12 |
|-------|----|-----|-----|-----|-----|-----|------|------|------|------|------|------|
| N | 12 | 140 | 234 | 408 | 560 | 736 | 1026 | 1260 | 1518 | 1924 | 2240 | 2580 |
| n_1 | 3 | 10 | 13 | 17 | 20 | 23 | 27 | 30 | 33 | 37 | 40 | 43 |
| n_2 | 4 | 14 | 18 | 24 | 28 | 32 | 38 | 42 | 46 | 52 | 56 | 60 |

- [2] Y. Dong, Y. Zheng, S. Li, C.-C. Li, X.-D. Chen, G.-C. Guo, and F.-W. Sun, *npj Quantum Inf.* **4**, 3 (2018).
- [3] J. Zopes and C. Degen, *Phys. Rev. Appl.* **12**, 054028 (2019).
- [4] A. M. Souza, G. A. Álvarez, and D. Suter, *Phys. Rev. Lett.* **106**, 240501 (2011).
- [5] E. D. Herbschleb, H. Kato, Y. Maruyama, T. Danjo, T. Makino, S. Yamasaki, I. Ohki, K. Hayashi, H. Morishita, M. Fujiwara, et al., *Nat. Commun.* **10**, 3766 (2019).
- [6] J. Nocedal and S. J. Wright, *Numerical Optimization* (Springer, New York, 2006).